

Impedance-Matched Differential Superconducting Nanowire Detectors

Marco Colangelo^{1,*}, Boris Korzh^{2,†}, Jason P. Allmaras^{2,3}, Andrew D. Beyer²,
 Andrew S. Mueller^{2,3}, Ryan M. Briggs², Bruce Bumble², Marcus Runyan²,
 Martin J. Stevens⁴, Adam N. McCaughan⁴, Di Zhu¹, Stephen Smith⁵, Wolfgang Becker⁶,
 Lautaro Narváez⁷, Joshua C. Bienfang⁸, Simone Frasca², Angel E. Velasco²,
 Edward E. Ramirez^{2,9}, Alexander B. Walter², Ekkehart Schmidt², Emma E. Wollman²,
 Maria Spiropulu⁷, Richard Mirin⁴, Sae Woo Nam⁴, Karl K. Berggren¹ and Matthew D. Shaw²

¹*Department of Electrical Engineering and Computer Science, Massachusetts Institute of Technology, Cambridge, Massachusetts, USA*

²*Jet Propulsion Laboratory, California Institute of Technology, 4800 Oak Grove Drive, Pasadena, California, USA*

³*Applied Physics, California Institute of Technology, 1200 East California Boulevard, Pasadena, California, USA*

⁴*National Institute of Standards and Technology, Boulder, Colorado, USA*


⁵*Cosmic Microwave Technology, 15703 Condon Avenue, Lawndale, California, USA*

⁶*Becker & Hickl GmbH, Nahmitzer Damm 30, Berlin, Germany*

⁷*Division of Physics, Mathematics and Astronomy, California Institute of Technology, Pasadena, California, USA*

⁸*National Institute of Standards and Technology, Gaithersburg, Maryland, USA*

⁹*California State University, Los Angeles, California, USA*

 (Received 16 December 2021; revised 7 February 2023; accepted 20 March 2023; published 28 April 2023)

Superconducting nanowire single-photon detectors (SNSPDs) are the highest-performing photon-counting technology in the near-infrared region. Because of delay-line effects, large-area SNSPDs typically trade off timing resolution and detection efficiency. This unavoidable fundamental constraint might limit their future deployment in demanding scientific applications. Here we introduce a detector design based on transmission-line engineering and differential readout for device-level signal conditioning, enabling a high system detection efficiency and a low detector jitter simultaneously. To make our differential detectors compatible with single-ended time taggers, we also engineer analog differential-to-single-ended readout electronics, with minimal impact on the system timing resolution. Our best niobium nitride differential SNSPD achieves a system detection efficiency of $(83.3 \pm 4.3)\%$ at 1550 nm and $(78 \pm 5)\%$ at 775 nm. The lowest system jitter is 13.0 ± 0.4 ps at 1550 nm and 9.7 ± 0.4 ps at 775 nm, limited by intrinsic contributions. These detectors also achieve sub-100-ps timing response at 1/100 of the maximum level, 30.7 ± 0.4 ps at 775 nm and 47.6 ± 0.4 ps at 1550 nm, enabling time-correlated single-photon counting with high-dynamic-range response functions. Furthermore, because of the differential impedance-matched design, our detectors exhibit delay-line imaging capabilities and photon-number resolution. The properties and high-performance metrics achieved by our system make it a versatile photon-detection solution for quantum computing, quantum communication, and many other scientific applications.

DOI: [10.1103/PhysRevApplied.19.044093](https://doi.org/10.1103/PhysRevApplied.19.044093)

I. INTRODUCTION

Superconducting nanowire single-photon detectors (SNSPDs) are the preferred photon-counting technology in the near-infrared region. Specialized SNSPD designs can achieve 98% efficiency at telecom wavelengths [1], ultralow intrinsic dark count rates [2,3], single-element

count rates greater than 100 Ms^{-1} [4], intrinsic timing jitter as low as 2.6–4.3 ps, depending on the wavelength [5], and intrinsic photon-number resolution [6]. Combining several of these metrics into a single device is desirable in many quantum communication applications [7], such as long-distance [8,9] and high-clock-rate [10,11] quantum key distribution, quantum teleportation [12,13], entanglement swapping [14], and multiplexed single-photon generation [15]. Detectors excelling in several metrics can also have a huge impact in other fields, such as laser ranging [16], low-power optical-waveform capture

*colang@mit.edu

†bkorzh@jpl.caltech.edu

[17], fluorescence-lifetime imaging [18], time-domain diffuse correlation spectroscopy [19], and deep-space optical communication [20].

One of the main challenges is the combination of an active area large enough for efficient coupling to a single-mode fiber together with low-jitter operation. The pulse propagation delays induced by the low phase velocity in long nanowires can contribute several tens of picoseconds to the uncertainty of the timing of the readout signal [21,22]. Therefore, large-area detectors with high detection efficiencies do not typically exhibit timing resolution of a few picoseconds. This fundamental trade-off ultimately limits the deployment of traditional-design SNSPDs in demanding scientific experiments.

Another challenge stands in the way of the introduction of low-jitter SNSPDs into applications. Although a few detector designs achieve sub-10-ps timing resolution, high-bandwidth oscilloscopes are typically used to characterize only the detector jitter [5,23]. In real applications, detectors are deployed with readout electronics that tend to degrade the overall system jitter. Therefore, to achieve excellent system timing resolution, the introduction of high-performance time tagging [24] and signal conditioning is also critical.

To address the combination of a large active area and low-jitter operation, in this work we engineer impedance-matched devices in a differential readout configuration. Our device inherits its base elements from the superconducting nanowire single-photon imager (SNSPI) [21]. The SNSPI was originally designed to provide micrometer-level spatial resolution based on the timing information of photon-detection pulses. Here we adopt its two-ended impedance-matched readout scheme. However, we do not use it for the reconstruction of an image from time-multiplexed pixels but we engineer the readout elements to improve the timing performances of a single-pixel SNSPD [25]. Our impedance-matching tapers are specifically designed to achieve a superior signal-to-noise ratio, and minimize reflections and distortions at the device level [26]. Here, the differential readout architecture, originally applied to lumped devices [22], is integrated with an impedance-matched single pixel and engineered to cancel the geometric delay-line contributions to the timing jitter. This optimized architecture provides a path to low-jitter, large-area single-pixel designs, breaking the existing trade-off between these design variables.

The impedance-matched differential architecture of this device offers additional advantages. The original SNSPI capabilities are partially preserved. By using the differential readout to determine the coordinate of the detection event [21], we achieve delay-line imaging capabilities. Moreover, our impedance-matched differential detectors achieve photon-number-resolution capabilities up to three photons, following our previous proof of concept with a single-ended device [6].

For optimal operation, this detector architecture would require two high-performance low-jitter time taggers, which is impractical at scale; to overcome this limitation, we design a differential-to-single-ended readout system based on analog electronics, which automatically cancels the geometric contribution and minimizes the overall system jitter. The pulses are first amplified and conditioned through analog electronics. The processed pulse is then fed to a time-correlated-single-photon-counting (TCSPC) module that completes the tagging operation and outputs a time tag with the delay-line contribution compensated. Our readout scheme makes the differential detector compatible with traditional single-ended readout systems while maintaining the advantages of the optimized architecture.

In Fig. 1(a) we show an optical micrograph of one of our impedance-matched differential detectors before packaging. The detector is fiber-coupled through a self-aligned packaging method using lollipop-shaped dies [27]. The superconducting tapers, interfacing the nanowire with the 50- Ω readout, extend along the die. The superconducting nanowire is arranged as a meander and is embedded in an optical cavity with a gold reflector to maximize photon absorption [Fig. 1(a), insets (i) and (ii)]. See Appendix A for details of the microwave design and Appendix C for details of the fabrication. Figure 1(b) shows a sketch of the overall architecture of our detection system. The impedance-matched nanowire meander is laid out in a differential configuration. A detection event generates a positive pulse and a negative pulse, V_{pos} and V_{neg} , respectively. The pulses are amplified and processed to produce their difference, V_{diff} , which is then fed to a single-ended TCSPC module, extracting a time tag t_{diff} with the jitter compensated for geometric contributions.

By combining our impedance-matched differential SNSPD with cryogenic differential-to-single-ended readout electronics and a time-to-analog-based time tagger, we achieve system jitter as low as 7.3 ± 0.3 ps full width at half maximum (FWHM) for straight nanowires. For nanowire devices with active areas larger than $15 \times 10 \mu\text{m}^2$, we achieve system detection efficiency higher than 45% at both 775 nm and 1550 nm. The FWHM system jitter is 9.7 ± 0.4 ps and 13.1 ± 0.4 ps, respectively. With the same measurement setup, we also achieve a state-of-the-art timing response at 1/100 of the maximum level [full width at 1/100 of the maximum (FW1/100M)].

The delay-line imaging capabilities of our detectors are particularly useful to identify the nature of the source of illumination, to debug fiber-coupling alignment, assess fabrication yield, estimate upper bounds for detection efficiency, and determine the effective signal velocity in the detector. The photon-number-resolution capabilities enable further applications, making this detector extremely versatile for several measurement scenarios.

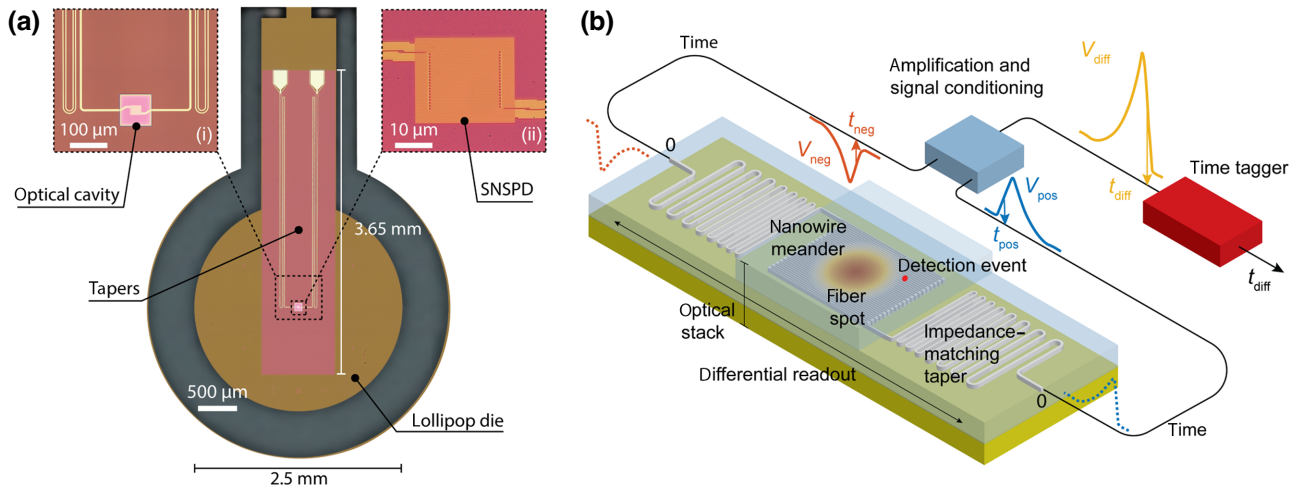


FIG. 1. Differential single-pixel superconducting nanowire single-photon detector. (a) Optical micrograph of a representative device. The detector die (lollipop) is connected to the parent wafer before packaging. Inset (i) shows an optical micrograph of the detector. The nanowire is embedded in an optical cavity to increase the detection efficiency. Inset (ii) shows an optical micrograph of the detector active area. (b) Artistic sketch of the SNSPD architecture realized in this work. Each meander end is interfaced with the readout through an impedance-matching taper. Note that the proportions of the elements in the figure are not to scale.

This paper is organized as follows. In Sec. II we discuss our design approach. We show how our optimized architecture can break the trade-off between high system detection efficiency and low detector jitter in traditional SNSPD designs (Sec. II A). We also discuss readout electronics and measurement setups that preserve the detector timing resolution at the system level (Sec. II B). Implementation of the design and characterization of detector performance are presented in Sec. III. We show the detector output pulse and discuss, compare, and validate the time-tagging procedure (Sec. III A). We then present the metrics achieved for the system detection efficiency, and we correlate the results to the alignment of the fiber spot on the active area, exploiting the imaging capabilities of the detector (Sec. III B). We then discuss the detector and system timing resolution (Sec. III C), and we show how our detector achieves photon-number resolution (Sec. III D). A general discussion of the results is given in Sec. IV. Finally, in Sec. V, we present a summary of the work and discuss applications and the scientific impact of the detector.

II. APPROACH

In the following, we propose an alternative design based on the microwave engineering of superconducting nanowires, enabling high system detection efficiency and low detector jitter at the same time (Sec. II A), overcoming the limitation of traditional devices. We then discuss how specialized readout electronics can be used to preserve timing resolution at the system level (Sec. II B).

A. Device design: Impedance-matched differential SNSPD

Single-pixel SNSPDs are traditionally modeled as lumped elements where the nanowire, usually a meander covering tens of square micrometers, behaves as a photon-triggered time-dependent resistor in series with a kinetic inductor [28]. Although providing a first-level description of the electrothermal dynamics, this picture does not consider the pulse propagation dynamics in the meander [29]. To achieve an optimal design, microwave properties need to be accounted for.

To illustrate the distributed effects in SNSPDs, we consider a simple model resembling the architecture presented later in this paper. A 100-nm-wide nanowire is arranged as a $20 \times 25 \mu\text{m}^2$ meander with a fill factor of 20%. The nanowire is assumed to have a sheet kinetic inductance of 80 pH per square and it is embedded in a cavity with a top-side dielectric stack and a backside metallic gold mirror. See Appendix C for more details on the cavity material and design. In this environment, the nanowire behaves like a stripline with characteristic impedance $Z_0 = 3.26 \text{ k}\Omega$ and effective microwave index $n_0 = 73.6$. The phase velocity $v_{\text{ph}} = 4.1 \mu\text{m}/\text{ps}$, and a pulse takes approximately 250 ps to travel between the two ends of the detector. See Appendix A for details on the microwave properties of nanowire-stripline architectures.

In conventional readout designs, this SNSPD would be configured for single-ended readout with a 50- Ω radio-frequency (rf) low-noise amplifier on one side and termination to ground on the other side. Figure 2(a) shows the simulation of detection pulses out of the SNSPD in this condition. The simulation includes both the electrothermal

evolution of the hotspot and the microwave dynamics of the nanowire [28]. See Appendix B for additional details on the simulations. The voltage pulses are characterized by several reflections and distortions caused by the impedance mismatch on both sides of the nanowire, which leads to a reduced slew rate and to a higher impact of the readout electrical noise on the timing jitter (j_{amp}) [5,30]. The relative variance in the propagation delays generated by detection events in different areas of the meander [different curves in Fig. 2(a)] appears as an additional uncertainty on the pulse time tag, referred to as “longitudinal geometric jitter” j_{geom} [22].

For detectors large enough to couple to a single-mode fiber [27], the geometric jitter can contribute on the order of tens of picoseconds to the total system jitter. Therefore, a trade-off between system detection efficiency and jitter must typically be made. In practice, as shown in the simulation in Fig. 2(a), the partial reflection from the termination to ground creates a local feature on the rising edge of the pulse (dashed circle), which acts as a partial compensation for j_{geom} . The compensation feature on the rising edge was previously reported in Ref. [31], and was described as a pulse-echoing effect due to impedance mismatch. Here we recognize that this effect might explain the compensation of the geometric jitter in traditional detectors. Triggering at this optimal level produces a time tag with the geometric contribution partially compensated for, meaning the timing resolution can be significantly greater than in the worst-case scenario of the full propagation delay (250 ps in this example). Nevertheless, this compensation feature is strongly dependent on other elements of the SNSPD design (e.g., pad layout, printed circuit board, and ground termination) and does not always guarantee optimal timing resolution. Moreover, this treatment applies only for detectors in a distributed regime. In single-pixel designs with fully lumped behavior (the delay-line effect can be ignored) [5,23], the jitter is mainly limited by intrinsic contributions and electrical noise.

Timing jitter arising from readout noise (j_{amp}) can be mitigated by designing the SNSPD to preserve the integrity of the output pulse. To avoid the reflections caused by the impedance mismatch at the readout port, an impedance-matching taper interfacing the approximately-kilo-ohm-impedance nanowire with the 50- Ω readout can be integrated. Because of the impedance transformation, the output pulse has a higher amplitude and a faster slew rate, allowing a reduction of the contribution of electrical noise to the timing jitter through a higher signal-to-noise ratio (SNR) [26]. The simulation result in Fig. 2(b) shows that the integration of a 200-MHz-cutoff Klopfenstein taper increases the output amplitude by a factor of 3.3 compared with the unmatched version in Fig. 2(a). This intrinsic amplification is in agreement with previous experimental demonstration [26]. The pulse rising edge is affected by

just one reflection due to the ground termination. The geometric effect of the transmission line is present, but the ground reflection still provides the local feature where j_{geom} is partially compensated.

The geometric jitter can be compensated in an active fashion with use of a differential readout configuration [22]. If the pulses coming from the two ends can be collected, straightforward signal processing allows one to remove any dependence on the location of the hotspot along the nanowire, effectively reducing the timing jitter through the compensation of the geometric contribution. Assuming the transmission line has a constant velocity v_{ph} , the time tags from the two ends are $t_{\text{pos}} = t_p + x_p/v_{\text{ph}}$ and $t_{\text{neg}} = t_p + (L - x_p)/v_{\text{ph}}$, respectively, where t_p is the detection time and x_p is the hotspot location. The normalized sum of the time tags t_{Σ} is independent of the detection location, and its jitter j_{Σ} will be unaffected by the geometric contribution.

To achieve the optimum geometric jitter cancellation and signal integrity, we use both a differential readout and impedance-matching tapers on both ends of the detector.

Figure 2(c) shows the simulation results for a differential detector with matched readout. The complementary output pulses, V_{pos} and V_{neg} , show no reflections and both have a slew rate superior to that of the unmatched pulse. To cancel the geometric jitter, one could postprocess the time tags of the complementary pulses, which also makes it possible to obtain information regarding the photon-absorption location, which is demonstrated in the following sections. Equivalently, as shown in Fig. 2(d), partial cancellation of the geometric contribution can be achieved by processing the difference of the complementary pulses V_{diff} , if the photon-absorption location is not required.

B. Readout design: Differential to single ended

To achieve the optimum timing resolution, we use a differential detector in combination with a high-resolution real-time oscilloscope, which serves as a time tagger. The two ends of the SNSPD are directly fed to the input of the oscilloscope after amplification [Fig. 3(a)]. The electrical-noise jitter is minimized through the use of cryogenic rf amplifiers at each end. The trigger voltage V_{th} is set such as to minimize the noise contribution, by sampling the steepest point of the pulse [5].

If the detection event happens at the exact center of the SNSPD [left side of the sketch on the right in Fig. 3(a)], and the system is perfectly balanced, there will be no geometric contribution, and $t_{\text{pos}} = t_{\text{neg}} = t_{\Sigma}$. When the detection event happens elsewhere [right side of the sketch on the right in Fig. 3(a)], the pulses arrive with a relative delay induced by the transmission-line effect. In this case, t_{Σ} can be processed and used to compensate for the

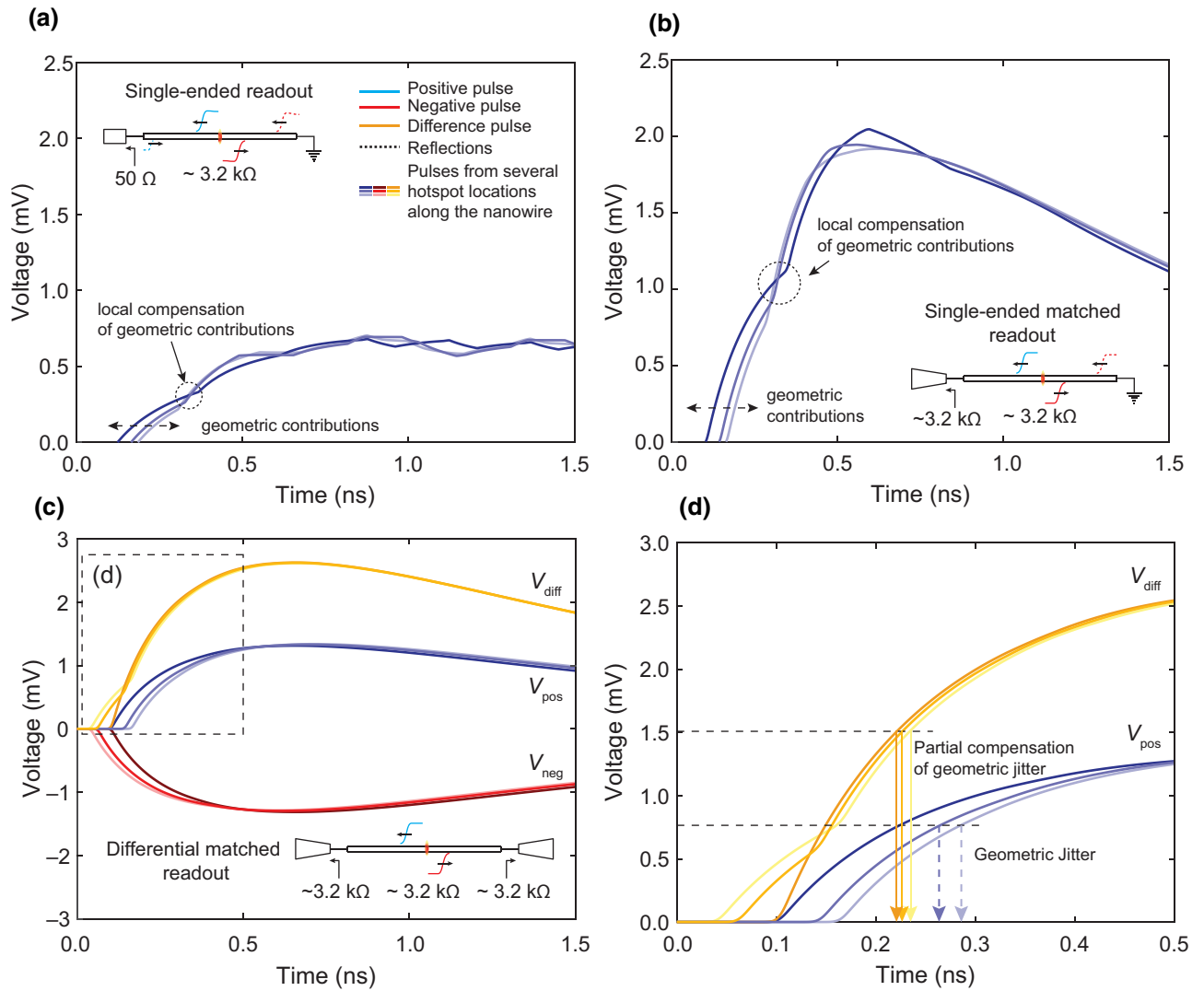


FIG. 2. Simulated SNSPD dynamics in several readout configurations. For (a)–(d), the shading of the curves (dark to light) indicates the pulses generated by photon absorption in different locations of the meander (near the center to near the edge). The schematics shown in the insets in (a)–(c) show the simulated readout setups. For simplicity, the nanowire meander is pictured as a straight wire. The blue (red) lines indicate the positive (negative) pulses generated by the photon absorption in the wire. The dashed lines indicate the reflection of the original pulses generated by impedance mismatch. (a) The SNSPD is configured for single-ended readout. (b) The SNSPD is configured for an impedance-matched single-ended readout. (c) The SNSPD is configured for an impedance-matched differential readout. (d) A partial cancellation of the geometric contribution can be achieved by processing the difference of the complementary pulses, V_{diff} .

geometric jitter contribution as illustrated in Fig. 3(a). The jitter associated with t_{Σ} , j_{Σ} , represents the jitter of the detecting element alone, e.g., the detector jitter.

For practical single-photon-counting applications, an instantaneous measurement is required, and the use of two low-jitter time taggers for each differential detector becomes impractical in many situations. To overcome this limitation, we design two readout schemes that make the differential detector compatible with a single-ended TCSPC module while maintaining the advantages of differential compensation of the geometric jitter. Figures 3(b) and 3(c) shows a comparison of the two approaches.

As shown in the simulation in Sec. II A, compensation of the geometric jitter can be obtained by processing the difference of the complementary pulses V_{diff} . In Fig. 3(b), we illustrate how, instead of postprocessing two individual time tags, t_{pos} and t_{neg} , to obtain t_{Σ} , a 2:1 balun transformer can be used to perform an operation equivalent to an analog difference of the complementary pulses. After amplification, the two sides of the detector are connected to the differential inputs of the balun, with the output being sent to a TCSPC module. The module outputs a time tag t_{diff} . The threshold voltage of the module can be set to minimize the spread of the time-tag distribution, corresponding

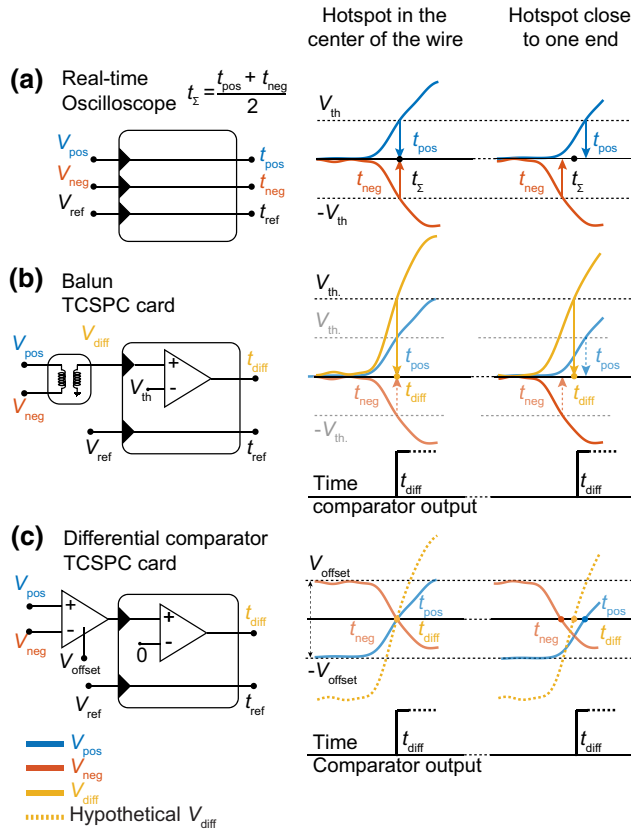


FIG. 3. Various differential single-pixel readout setups and pulse processing. The pulses are shown for two arbitrary hotspot locations along the meander. (a) A high-resolution real-time oscilloscope is used to collect the complementary pulses. (b) The complementary pulses are fed, after amplification, to the differential input of a balun that performs an operation equivalent to an analog difference of the pulses. (c) The complementary pulses are fed, after amplification, to the input of a differential comparator.

to the condition $t_{\text{diff}} \approx t_{\Sigma}$. The jitter extracted with this method, j_{diff} , represents the timing resolution of the whole measurement system, the system jitter. Because of the insertion loss (6 dB) of the balun, we expect the system jitter j_{diff} to be slightly degraded compared with the detector jitter j_{Σ} .

Figure 3(c) illustrates the use of a differential comparator, or equivalently, a differential-input TCSPC module. In

this case, the differential comparator automatically cancels the geometric jitter, and no transformation of the pulses is required. To achieve optimum cancellation, a positive (negative) offset is provided to the negative(positive) pulse at the input of the differential comparator. When the difference between the two inputs becomes positive, the comparator generates a digital signal, with a rising-edge slope limited by the slew rate of the comparator. This digital signal is time tagged by the TCSPC module, producing the time tag t_{diff} . The offset voltage can be set to minimize the spread of the time-tag distribution, matching the condition $t_{\text{diff}} \approx t_{\Sigma}$. This approach does not introduce insertion loss, and thus it could be preferred over the 2:1 balun transformation in certain situations.

III. RESULTS

In the following, we describe the experimental implementation and results of the approaches proposed in the previous sections.

A. Impedance-matched differential detectors

Our impedance-matched differential designs are realized with niobium nitride (NbN). Optical micrographs of the detectors are shown in Fig. 1(a). Details of the fabrication process are reported in Appendix C. We characterize SNSPDs from several fabrication runs, each with different designs and specifications, as well as two variants of niobium nitride. The variants are identified with the institution where the deposition was performed, i.e., at the Massachusetts Institute of Technology (MIT) or at the Jet Propulsion Laboratory (JPL). In Table I, we summarize the main characteristics of a selected subset of detectors, representative of the wide design-parameter space.

All of the reported detectors reach saturation of the internal detection efficiency and are operated on the system-detection-efficiency plateau. The detectors with MIT-grown NbN have a slightly lower switching current (I_{sw}) than those with JPL-grown NbN for same nominal thickness. Overall, the detector switching currents range between 14 and 25 μA .

Figure 4(a) shows the complementary pulses from device A (see Table I) biased with 14 μA (96 of I_{sw})

TABLE I. Characteristics of a subset of devices representative of the design space. The size of the device is also reported as the number of squares, which is useful to calculate the total inductance. As most of the inductance consists of the impedance-matching tapers, we also report the ratio of the inductance in the active area to the total inductance of the device as a percentage.

Device	Type	Width (nm)	Pitch (nm)	Active area (μm^2) or length (μm)	No. of squares	L ratio (%)	Cavity λ (nm)	Cavity	NbN variant	T_c (K)	I_{sw} (μA)
A	Meander	100	500	25×20	27 545	37	1550	Single	MIT	7.9	14.6
B	Meander	100	400	15×10	21 295	18.4	800	Double	JPL	6.8	22.0
C	Straight wire	120	...	25	17 603	1.2	1550	Single	MIT	7.9	22.0
D	Meander	100	500	22×15	24 215	28	1550	Double	JPL	6.4	20.0

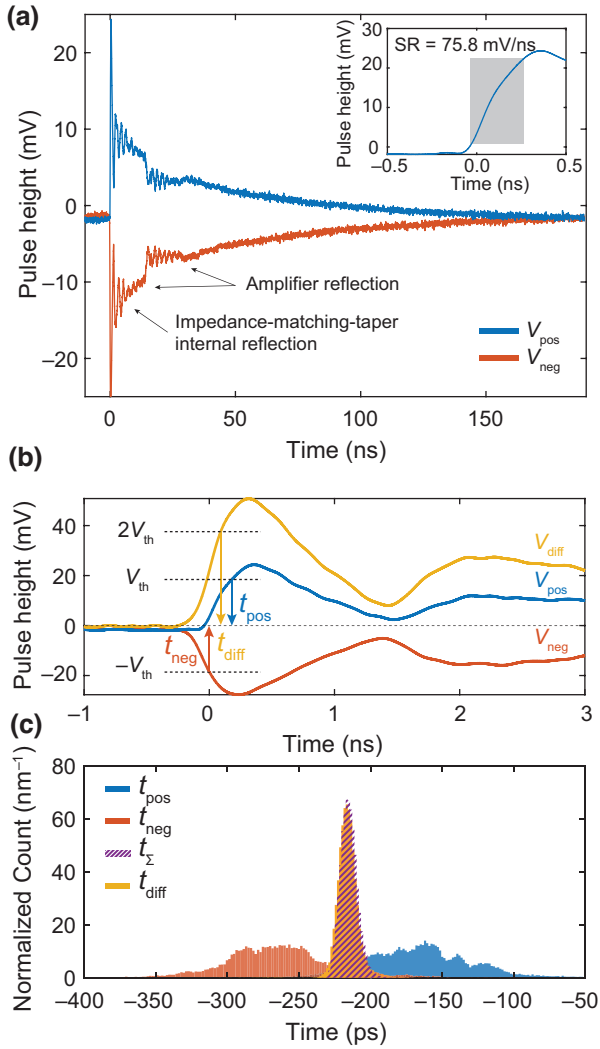


FIG. 4. (a) Complementary pulses from device A upon illumination. The main signal discontinuities are attributed to reflections from the low-noise amplifier. The high-frequency ripple is attributed to internal reflection in the impedance-matching taper due to the limited design bandwidth. The inset shows positive pulse slew rate (SR). The impedance-matching taper boosts the slew rate. (b) Time-tagging procedure for V_{pos} , V_{neg} , and V_{diff} . (c) Time-tag distributions for 123 348 detection events.

and illuminated with a laser having a central wavelength of 1550 nm, a pulse width of 1 ps, and a repetition rate of 10 MHz. The output pulses are amplified with two high-dynamic-range, 2-GHz cryogenic low-noise amplifiers (see Appendix D) and are acquired with an oscilloscope with a sample rate of $80 \times 10^9 \text{ s}^{-1}$. The slew rate is 75.8 mV/ns [see the inset in Fig. 4(a)], and the reset time is approximately 160 ns. The high-frequency ripple visible up to approximately 50 ns is due to the internal reflections in the matching tapers, while the reflections located between approximately 14 ns and approximately

30 ns are due to negative reflections from the low-noise amplifiers.

Figure 4(b) shows the time-tagging procedure for the complementary pulses as well as the timing of their difference, V_{diff} , as discussed in Sec. II B. As shown in Fig. 4(c), the t_{diff} distribution calculated for more than 100 000 detection events is substantially narrower than the individual distributions of t_{pos} and t_{neg} and is approximately equivalent to the t_{Σ} distribution. This demonstrates that the operation can be implemented with analog components as proposed in Sec. II B, and is discussed further in Sec. III C.

B. System detection efficiency and delay-line imaging capabilities

Figure 5 shows the system-detection-efficiency curves obtained for the devices selected for this paper. Detector A achieves 71% saturated system detection efficiency with a dark count rate of approximately 200 s^{-1} . The efficiency is limited by the detector fill factor (20%) and the absorption in the metallic mirror. Further investigations into the trade-off of the fill factor and microwave propagation in the active region of the differential SNSPD, as well as the use of a more-reflective metal for the mirror/ground layer, may lead to an increase of the system detection efficiency in the future. Detector B achieves 47.6% saturated detection efficiency at 775 nm with a dark count rate of approximately 100 s^{-1} . The single-wire geometry of detector C leads to 8.8% saturated detection efficiency at 1550 nm with a dark count rate of approximately 10 s^{-1} . The relative uncertainty on all system detection efficiencies is approximately 5.2%. See Appendix G for more details on this estimation. To explain the discrepancies between the detection efficiencies of detector A and detector B, we investigate the quality of the fiber alignment by exploiting the delay-line imaging capabilities of our detectors.

With a differential readout [21,22] the relative delay between the time tags of the complementary pulses $t_{\Delta} = t_{\text{pos}} - t_{\text{neg}} = (L_m - 2x_p)/v_{\text{ph}}$ encodes the spatial coordinate of the photon-detection location x_p on the nanowire [Fig. 6(a)]; L_m is the total length of the meander. In differential time-tag multiplexed SNSPD arrays and single-photon imagers [21,32] the pixels are separated by a fixed length of delay line or are part of a continuous delay line. The t_{Δ} histogram is used to determine the spatial distribution of the photon counts and to reconstruct the image.

Because of the striplinelike design of our differential detector, the signal propagation velocity is low enough to enable the use of t_{Δ} to precisely determine the photon-absorption locations along the nanowire meander. For the same detector model as in the previous section, the readout signal travels at a velocity of $4.1 \mu\text{m}/\text{ps}$ in the nanowire,

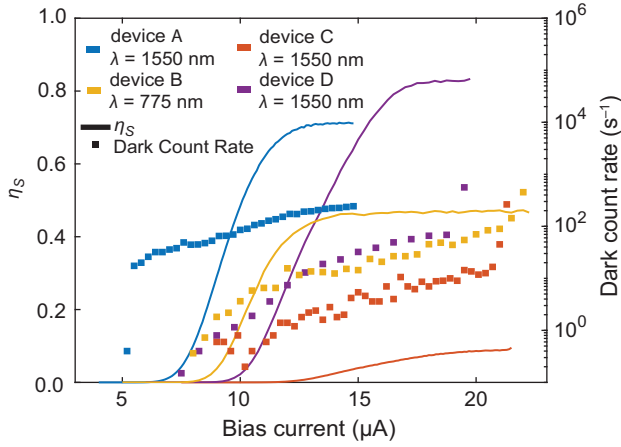


FIG. 5. System-detection-efficiency (η_S) curves for detectors A, B, C and D at 0.84 K. Solid lines indicate the system detection efficiency, and the markers indicate the dark count rate. All the detectors achieve saturation of the internal detection efficiency.

meaning that it takes approximately 6.1 ps for the signal to traverse a single meander. This delay can be resolved with high-resolution time taggers. Moreover, the monolithic impedance matching and the use of a cryogenic amplifier preserve the pulse leading edge, avoid distortions, and minimize the added electrical noise, which preserves the original timing information.

To showcase this method, we first simulate the imaging capability of the detector for the lowest-order mode LP₀₁ of a single-mode fiber at 1550 nm. The mode is assumed to land on the SNSPD without spreading or distortions, maintaining the same size as at the end of the fiber. Figure 6(c) shows the simulated distribution of the differential time t_Δ when the center of the optical mode coincides with the center of the detector [Fig. 6(b)]. Each subdistribution of the histogram corresponds to detection events from consecutive wires in the meander. Because the mode is aligned with the center of the meander, the spacing between adjacent subdistributions is constant, and the peak of the envelope of the overall t_Δ distribution (t_y) is located at 0 ps.

When the mode and the detector centers are misaligned [e.g., $\Delta x = 3 \mu\text{m}$ and $\Delta y = 5 \mu\text{m}$ in Fig. 6(d)], the histogram shows two characteristic features [Fig. 6(e)]. First, t_y does not coincide with $t_\Delta = 0$. t_y encodes the vertical shift relative to the detector center according to $\Delta y = t_y \frac{v_{\text{ph}}}{2} \frac{w}{W \times F}$, where w is the width of the nanowire, W the width of the meander active area, and F the fill factor of the meander. For clarity, the variables are also defined pictorially in Fig. 6(a). Second, the relative spacings between adjacent peaks, $\Delta t_{\Delta,1}$ and $\Delta t_{\Delta,2}$, are not identical. Their difference $t_x(\Delta x) = \Delta t_{\Delta,1} - \Delta t_{\Delta,2}$ encodes the horizontal offset of the events from the center of the meander according to $\Delta x = v_{\text{ph}} t_x / 8$. See Appendix E for the derivation of

these first-order formulas. In this specific case, $t_y (5 \mu\text{m}) = 118.3 \text{ ps}$ and $t_x (3 \mu\text{m}) = 5.8 \text{ ps}$.

When the mode is unknown, the difference time histogram can be used to reconstruct the spatial distribution of the light and identify the nature of the source and illumination conditions. When the mode is known, analysis of the t_Δ histogram is specifically useful to debug fiber-coupling alignment, assess fabrication yield, estimate upper bounds for detection efficiency, and determine the effective phase velocity of the detector. Figures 6(f) and 6(e) show direct exploitation of this method to check for mode alignment with the detector active area.

Figure 6(f) shows the t_Δ distribution for detector A illuminated with the 1550-nm pulsed laser fiber-coupled to the detector through a single-mode fiber. We fit the distribution with a Gaussian model to estimate the mode misalignment. For detector A, the misalignment is estimated to be $\Delta x = -0.01 \mu\text{m}$ and $\Delta y = 3.74 \mu\text{m}$. The fraction of the mode collected by the active area is 99.7%. This analysis confirms that the system detection efficiency is limited to approximately 70% at 1550 nm by the meander fill factor and the cavity design.

Figure 6(g) shows the t_Δ distribution for detector B illuminated with the 775-nm pulsed laser fiber-coupled to the detector through a single-mode fiber. In this case, inspection of the histogram reveals that the mode is strongly misaligned toward the lower corner of the meander. Combined with the smaller active area, the detector can reach only approximately 47% system detection efficiency. When the mode is aligned, the system detection efficiency should exceed 70%, on the basis of characterization of detector A. We verify this by packaging a detector with a larger active area ($30 \times 10 \mu\text{m}^2$) that relaxes the constraints on the fiber alignment. For this detector, the system detection efficiency is $(78 \pm 5)\%$.

We also characterize a detector with a double optical stack tuned to 1550 nm (device D). The system-detection-efficiency curve is shown in Fig. 5. Device D achieves $(83.3 \pm 4.3)\%$ system detection efficiency due to the double-cavity design and optimal alignment.

C. Detector jitter, system jitter, and FW1/100M

Figure 7(a) shows the detector jitter j_Σ and its dependence on bias current and wavelength for the detectors listed in Table I. The jitter is obtained as the FWHM of the exponentially modified Gaussian function used to fit the t_Σ distribution. The uncertainties are calculated as the 95% confidence bounds on the data. The jitter decreases for the shorter wavelength and for bias currents closer to the switching current, which indicates that the dominant contribution is the intrinsic jitter of the detector [5,33], demonstrating that the detector design succeeds in overcoming the effects of the geometric jitter and amplifier jitter to enable scalability to practical active areas. Detector

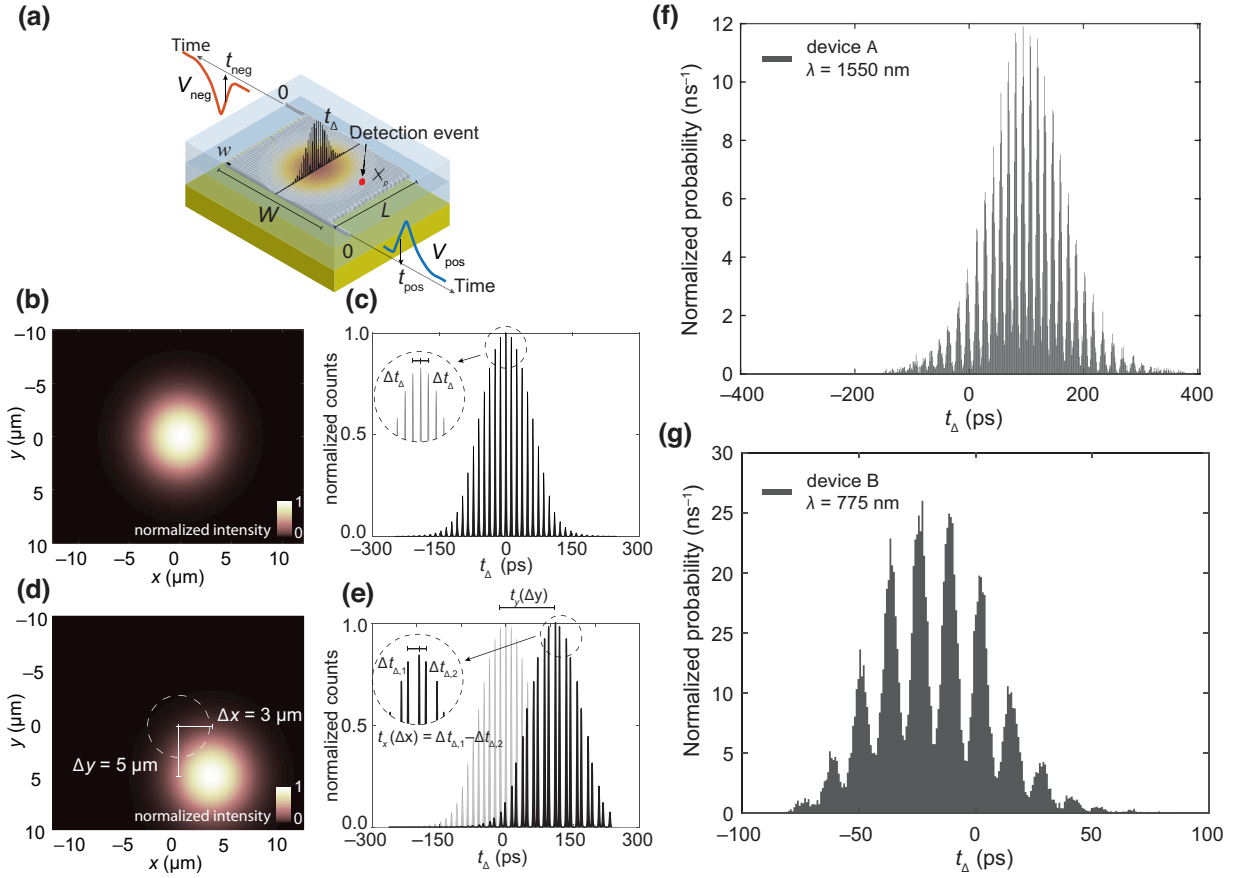


FIG. 6. Single-mode differential delay-line imaging. When differential readout is used and the speed of signal propagation is on the order of a few micrometers per picosecond, differential detectors can be used for localization of the light beam. (a) A single LP01 mode illuminates the center of an $L \times W$ -area meander with a w -wide nanowire. (b) The LP01 mode is aligned with the detector center. (c) Simulation of the differential time t_{Δ} histogram. (d) The LP01 mode and the meander centers are misaligned by $\Delta x = 3 \mu\text{m}$ and $\Delta y = 5 \mu\text{m}$. (e) Simulation of the differential time t_{Δ} histogram. (f) Differential time distribution t_{Δ} for detector A. (g) Differential time distribution t_{Δ} for detector B.

A achieves a detector jitter of 12.4 ± 0.6 ps at the target wavelength of 1550 nm and a detector jitter of 8.3 ± 0.3 ps at 775 nm. Detector B achieves a detector jitter of 9.4 ± 0.8 ps at its target wavelength of 775 nm. Detector C achieves a detector jitter of 12.1 ± 0.5 ps at 1550 nm. For 775-nm photons, it achieves the lowest detector jitter of 7.0 ± 0.3 ps, due to its straight-wire geometry, with minimal geometric contribution by design and the lowest probability of film defects, enabling operation at a higher fraction of the depairing current [34]. We expect that the intrinsic jitter of the straight-wire geometry can be reduced even further through the use of narrower wires (here approximately 120 nm) [5].

Figure 7(b)–7(e) compares the distribution of t_{Σ} with that of t_{diff} obtained with the methods described in Sec. II B using a TCSPC module (Becker & Hickl SPC-150NXX [35]) in combination with a balun or a cryogenic differential comparator (see Appendix D). The proposed acquisition schemes achieve j_{diff} only 3%–6% higher than j_{Σ} , demonstrating that both methods achieve effective

cancellation of the geometric jitter equivalent to the oscilloscope-based acquisition, while minimally affecting the overall timing resolution. The uncertainty on these values is mainly due to the resolution of the TCSPC module and is estimated as two time bins $\sigma_{\text{TCSPC}} = 0.4$ ps. This opens up the possibility of using the detection system for photon-counting applications with high detection efficiency and sub-10-ps system jitter, while operating at count rates in the megahertz range, which is not possible with oscilloscope-based data acquisition and which has not been achieved previously for the wavelengths in question.

In Fig. 7(a) we also show the results for the system jitter for device D. Note that, differently from detectors A, B, and C, detector D is tested with a balun and a TCSPC module, and the detector-facing cryogenic amplifiers are replaced with room-temperature amplifiers (details in Appendix D). The system jitter obtained is 13.0 ± 0.4 ps at 1550 nm. Note that, combined with the previous observations, these data highlight that cryogenic amplifiers are not essential to the jitter-cancellation methods; the SNR provided by

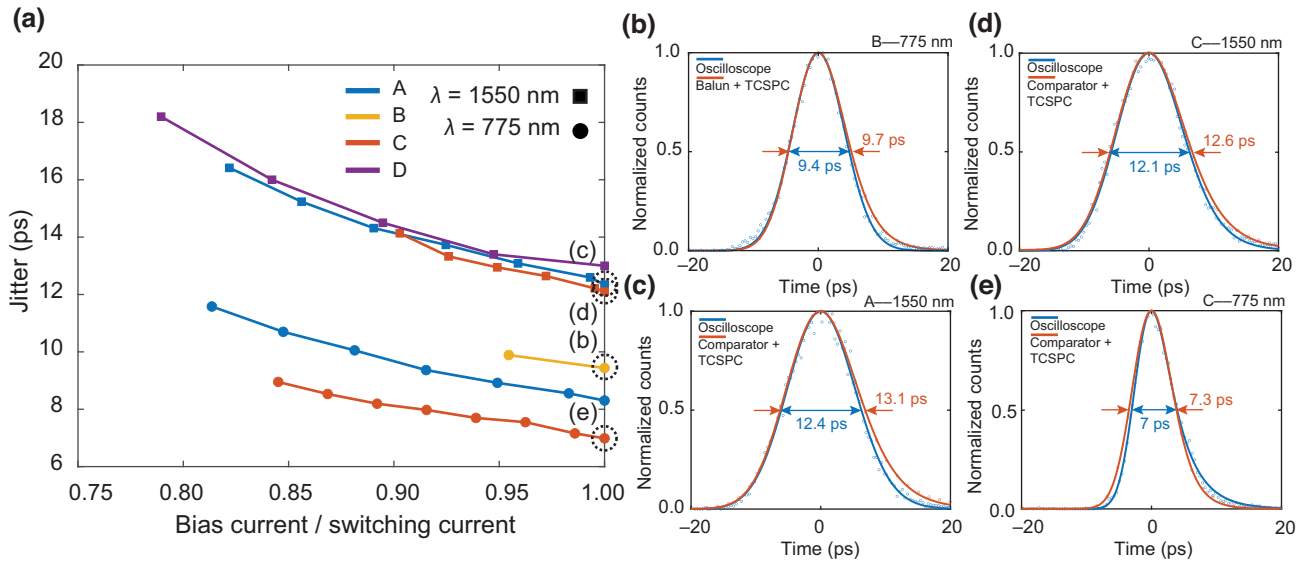


FIG. 7. (a) Dependence of the detector jitter, j_{Σ} , across several detectors designs, wavelengths, and bias currents. The trends indicate that the dominant contribution is intrinsic. (b)–(e) Histograms corresponding to the points indicated in (a). Comparison of detector jitter and system jitter obtained with the methods described in the paper. The system jitter obtained with the differential-to-single-ended readout is at most 6 greater than the detector jitter, showing that the additional readout electronics have a minimal impact on the overall timing resolution.

the impedance matching is sufficient. Delay-line imaging, however, requires cryogenic amplifiers in order to clearly resolve the peaks in the t_{Δ} histogram. In Table II we provide a final summary of the results presented above.

In applications such as quantum key distribution or pulse-position-modulated optical links, to achieve a low error rate and a high clock rate [8,11,36], an instrument response function with low spread over several orders of magnitude (high dynamic range) is required. In addition to a low timing jitter (FWHM of the timing response), this characteristic is quantified by FW1/100M of the instrument response function. In fluorescence-lifetime imaging, a large FW1/100M can limit the contrast, while in time-resolved spectroscopy, the dynamic range is affected [37, 38]. Figure 8 shows that our differential detector A, in combination with the differential comparator and the TCSPC module, achieves 47.6 ± 0.4 ps FW1/100M at 1550 nm, which is a factor of 4 lower than what has been achieved with free-running (In,Ga)As/InP single-photon avalanche diodes operating at the same wavelength [36]. At 775 nm, detector B combined with the balun and the TCSPC module, achieves 30.7 ± 0.4 ps FW1/100M, which is a factor of 7 lower than the best demonstration with red-enhanced silicon single-photon avalanche diodes [38]. These metrics position our differential detector for application in biomedical imaging [19,39], quantum communication [7], and laser ranging [16], where the most-stringent timing performance is required over a large dynamic range.

D. Photon-number resolution

Recently, it was demonstrated that the output-pulse amplitude of impedance-matched tapered SNSPDs can directly encode the number of photons detected simultaneously [6]. In the original superconducting tapered nanowire detector, the quasilumped nature of the photon-sensitive area and the single-ended readout make the pulse amplitude scale sublinearly with the photon-number-dependent

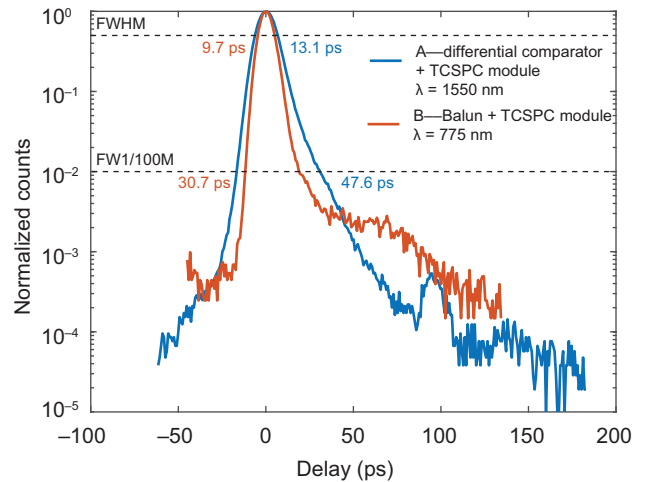


FIG. 8. Timing response for detector A at $\lambda = 1550$ nm in combination with the differential comparator and the TCSPC module, and for detector B at $\lambda = 775$ nm in combination with the balun and the TCSPC module.

TABLE II. Summary of experimental results. Note that device D is measured with a balun and a TCSPC module (and room-temperature amplifiers) only.

Device	η_S (%)	System jitter (oscilloscope) (ps)	Cancellation method	System jitter (method) (ps)	Difference (%)
A	71.0 ($\lambda = 1550$ nm)	12.4	Differential comparator	13.1	5.6
B	47.6 ($\lambda = 775$ nm)	9.4	Balun	9.7	3.2
C	8.8 ($\lambda = 1550$ nm)	12.1	Differential comparator	12.6	4.1
D	83.3 ($\lambda = 1550$ nm)	...	Balun	13.0	...

hotspot resistance $R_{HS}(n)$. Here the same simple picture can be applied, but the differential character of the detector encodes the photon-number information in the difference of the pulses from the two ends, V_{diff} .

We characterize the photon-number-resolution capability using an attenuated 1550-nm pulsed laser with a repetition rate of 1 MHz (see Appendix D for details of the measurement setup). Figure 9(a) shows a sample of representative traces of the difference of the output pulses for effective mean photon number $\tilde{\mu} = 0.73$. $\tilde{\mu}$ is estimated from the photon rate at the cryostat input port, scaled by the system efficiency (see Appendix F). The pulse-amplitude distribution sampled on the first peak [dashed line in Figure 9(a)] is shown in Fig. 9(b). Our detector can distinguish up to $n = 3$ photons. We fit the distribution using three Gaussian functions representing the number of photons. The separation between the one-photon distribution and the two-photon distribution is more than 9 standard deviations of the one-photon-distribution width $\sigma_{n=1}$ ($9\sigma_{n=1}$), making this detector suitable for application in quantum optics experiments. Note that transmission-line effects cause the amplitude and the shape of the differential output pulses to depend on the photon-landing location. The effect tends to increase the width of the amplitude distribution, with a larger impact for multiphoton events, where the relative distance between landing locations plays an additional role (see Appendix F). The additional features in the pulse (second and third peaks) might provide additional information and allow the resolution of higher photon numbers through signal processing.

IV. DISCUSSION

In this paper, we demonstrate that by redesigning the architecture of the SNSPD and with an appropriate read-out scheme, the trade-off between high detection efficiency and low system jitter can be overcome. The impedance-matched design enables photon-number-resolution capabilities, and the differential design enables intrinsic device-level imaging capabilities.

A limitation in the performance of the current design is the maximum count rate. Although we do not perform specific measurements to characterize this metric, we expect the count rate to be ultimately limited by the reset time of our detectors, approximately 160 ns. To address this issue,

an active quenching circuit could be coupled to the device [40] and integrated on-chip in future iterations.

The design approach we provide in this paper traces a path to the realization of detectors with high system detection efficiency and high timing resolution. Nevertheless, in the current demonstration, the performance is still below what could be achieved with designs focused on a single metric. For the system detection efficiency, assuming an optimal fiber alignment, the current limitations are attributed to the detector fill factor and the cavity design. Both design elements are selected solely to facilitate fabrication and design, and could be improved in future iterations.

The detector jitter we measure for our devices approaches the few-picosecond domain. Nevertheless, the values are still 2–3 times higher than the values obtained with specialized low-jitter devices. As discussed above, in our SNSPDs, the detector-jitter trends with respect to bias current and wavelength suggest that the dominant jitter contribution has an intrinsic nature [33]. Compared with the device with the current record for detector jitter

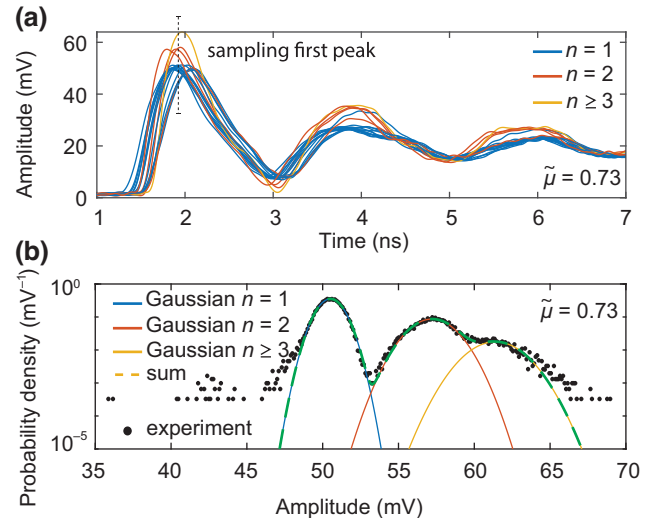


FIG. 9. Detector output and counting statistics under coherent-state illumination. (a) Sample of detector output V_{diff} for a pulsed laser with $\tilde{\mu} \approx 0.73$. The pulses are grouped and colored by pulse height. (b) Gaussian fitting of the pulse-amplitude histograms for $\tilde{\mu} \approx 0.73$, sampling the first peak [dashed line in (a)].

(4.3 ps at 1550 nm) [5], devices A and B feature larger areas. While the differential design effectively cancels the geometric contribution, large-active-area devices can be affected with a higher probability by defects induced by nanofabrication (e.g., line-edge roughness) or intrinsic to the film (e.g., natural constrictions and grain boundaries). The record-jitter device was operating at a 0.8 fraction of the critical depairing current (I_{dep}), while, on the basis of previous measurements [34], we expect our device to operate between $0.5I_{\text{dep}}$ and $0.7I_{\text{dep}}$. This explains the overall higher jitter values obtained in our meandered SNSPDs. Device C, although in a straight-wire configuration, has a switching current considerably suppressed compared with the reference record device. This could explain the higher jitter. In this demonstration, we do not explicitly focus on optimizing the fabrication and film quality. We expect that by improving these technical aspects in the future we will reach timing resolutions closer to the current record values.

The differential-to-single-ended setups rely on the use of external components (balun or differential comparator), either at room temperature or at cryogenic temperature. Although our experiments show that the system performance is minimally degraded compared with the detector-only performance, external components make the detector prone to added electrical noise, which can ultimately degrade the system jitter. To make the system more compact and improve the performance, similar electrical circuits could be custom designed, integrated and colocated on-chip with the impedance-matched differential detector. Moreover, niobium nitride nanowires are also used in cryoelectronics applications (e.g., x-Tron family [41,42]) and were recently exploited to realize compact microwave devices [43,44]. Design and monolithic integration of nanowire-based electronics for on-chip signal conditioning could significantly improve the system performances and avoid additional postprocessing (e.g., photon-number resolution).

V. SUMMARY AND CONCLUSION

Our impedance-matched differential detector, coupled with high-speed differential-to-single-ended readout, achieves high system detection efficiency and low system jitter while maintaining the convenience of single-ended readout. At 775 nm, we achieve 9.7 ± 0.4 ps FWHM and 30.7 ± 0.4 ps FW1/100M system jitter with $(47.3 \pm 2.4)\%$ system detection efficiency, limited by fiber alignment. With optimal alignment, this detector can achieve a system detection inefficiency greater than 70%. At 1550 nm, we achieve 13.1 ± 0.4 ps FWHM and 47.6 ± 0.4 ps FW1/100M system jitter with $(71.1 \pm 3.7)\%$ system detection efficiency. A detector with a double cavity achieves a system detection efficiency of $(83.3 \pm 4.3)\%$ and a system jitter of 13.0 ± 0.4 ps.

This performance may enable quantum communication at clock rates greater than 20 GHz, high-resolution single-photon laser ranging, faint optical-waveform reconstruction, and previously unachievable capabilities in biomedical imaging applications. The microwave design of our nanowire detectors combined with the differential readout architecture enables precise determination of the photon-absorption locations along the nanowire meander, unlocking delay-line imaging capabilities. We exploit this property to image the fiber mode projected on the detector and verify the fiber alignment. Our detectors also achieve photon-number resolution up to three photons. The possibility of discriminating the number of photons from optical radiation with high efficiency and timing resolution will enable the use of our detectors in applications such as nonclassical state generation [15,45], novel protocols in quantum networking [46,47], and quantum information processing and linear optical quantum computing [48–50].

Our prototype detectors are currently in use in single-photon LIDAR [51] experiments and quantum information processing [52], and are proposed as an experimental platform to probe fundamental superconducting nanowire switching phenomena [53].

ACKNOWLEDGMENTS

This research was sponsored in part by the Army Research Office and was accomplished under Cooperative Agreement No. W911NF-16-2-0192 and W911NF-21-2-0041. The views and conclusions contained in this document are those of the authors and should not be interpreted as representing the official policies, either expressed or implied, of the Army Research Office or the U.S. Government. The U.S. Government is authorized to reproduce and distribute reprints for Government purposes notwithstanding any copyright notation herein. Support for this work was provided in part by the Defense Advanced Research Projects Agency Defense Sciences Office DETECT and Invisible Headlights programs, the NASA Spacecraft Communication and Navigation technology development program, the Alliance for Quantum Technologies Intelligent Quantum Networks and Technologies research program, and the National Science Foundation under Contract No. ECCS102000743. D.Z. acknowledges support from the National Science Scholarship from A*STAR, Singapore, and a Harvard Quantum Initiative Postdoctoral Fellowship. J.P.A. acknowledges support from a NASA Space Technology Research Fellowship. A.B.W. acknowledges support from the NASA Postdoctoral Program at the Jet Propulsion Laboratory. Part of this research was performed at the Jet Propulsion Laboratory, California Institute of Technology, under contract with NASA. The authors thank S. Weinreb and J. Bardin for useful technical discussions, J. Daley and M.K. Mondol of the MIT Nanostructures Laboratory Facility for technical support, and P. Keathley, M.

Bionta, and A. Bechhofer for assistance in editing the final manuscript.

M.C. and B.K. conceived, designed, and performed the experiments. M.C., A.D.B., B.B., and R.M.B. fabricated the devices. M.C. performed the simulations. M.C., B.K., and J.P.A. analyzed the data. M.C., A.D.B., B.K., J.P.A., A.S.M., R.M.B., B.B., M.R., M.J.S., A.N.M., D.Z., S.S., W.B., L.N., J.C.B., S.F., A.E.V., E.E.R., A.B.W., E.S., E.E.W., M.S., R.M., and S.W.N. contributed materials and/or analysis tools. K.K.B. and M.D.S. supervised the project. M.C. and B.K. wrote the paper with inputs from all authors.

APPENDIX A: MICROWAVE DESIGN

Here we discuss the microwave design for our detector optimized for 1550-nm radiation. The superconducting nanowire is embedded in an $\text{SiO}_2/\text{TiO}_2$ optical cavity with a bottom metallic reflector. The silicon oxide layer separating the nanowire from the reflector is 243 nm thick, and forms a stripline structure with the reflector acting as a ground plane. In Fig. 10 we show the simulation of the characteristic impedance and phase-velocity factor for the full nanowire stripline. The geometric parameters are shown in the cross-section sketch. If we assume a niobium nitride sheet kinetic inductance $L_k = 80$ pH per square (typical of a 7-nm-thick layer), a 100-nm-wide wire has characteristic impedance $Z_0 = 3261 \Omega$ and phase velocity 1.36% of the speed of light.

As explained in Sec. II, to preserve the signal-to-noise ratio and the timing information of the output pulses, microwave impedance matching is required. We design and monolithically integrate two Hecken tapers, one for each side of the differential nanowire [Fig. 1(a), inset

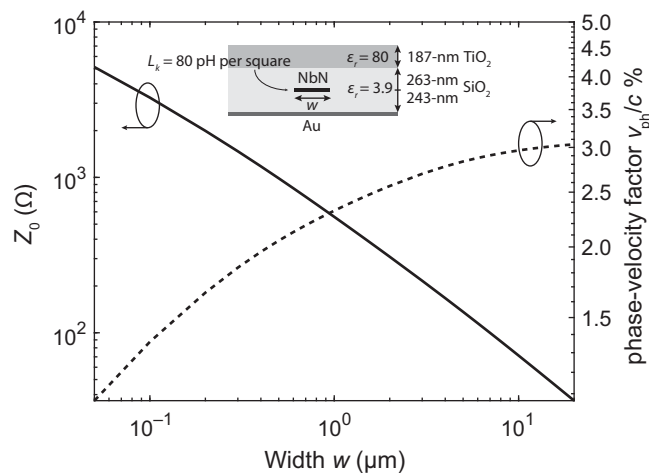


FIG. 10. Simulation of the nanowire-stripline parameters: characteristic impedance and phase-velocity factor versus conductor width for a sheet kinetic inductance $L_k = 80$ pH per square.

(i)]. The tapers are designed with the computer-aided-design-layout software program PHIDL [54]. To reduce the length of the taper and the fabrication complexity, we start the matching from a width of 300 nm. The 300-nm and 100-nm wire sections are connected through optimal curves [Fig. 1(a), inset (ii)]. The tapers have a total length of 7.6 mm with 8648 squares, a kinetic inductance of $0.69 \mu\text{H}$, and a lower cutoff frequency of 537 MHz, and introduce a 0.93-ns delay. For the MIT devices, the layout is patterned with a positive-tone resist, therefore resembling a grounded-coplanar-waveguide geometry after etching. Because the width of the slot of the coplanar waveguide is 1 order of magnitude larger than the thickness of the silicon oxide layer, the structure behaves approximately as a stripline and the side grounds can be ignored.

APPENDIX B: SPICE SIMULATION

We simulate the impedance-matched differential detector using a SPICE model that incorporates both the electrothermal feedback of the nanowire and the microwave dynamics of the line. The SPICE model of the SNSPDs was implemented by Berggren *et al.* [28] on the basis of the phenomenological hotspot velocity model of Kerman *et al.* [55]. The nanowire transmission line is simulated by our using a SPICE lossy-transmission-line model (LTRA) with capacitance per unit length and inductance per unit length values reproducing the impedance and phase velocity of the line ($L = 800.6 \mu\text{H}/\text{m}$ and $C = 75.27 \text{ pF}/\text{m}$). We do not include any loss term. The taper is modeled as a cascade (300 sections) of transmission-line sections with varying impedance and phase velocities unique to each section. To simulate photon detection in different sections of the meander line, we change the length of the nanowire transmission line. In the example in Fig. 11, we assume

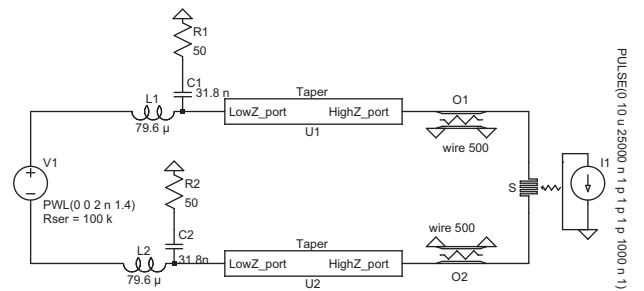


FIG. 11. Schematics of the SPICE simulation for an impedance-matched differential detector. The taper is modeled as cascaded transmission lines (300 sections) with varying impedance and phase velocities unique to each section. The nanowire is simulated as a lossy transmission line (LTRA) with $L = 800.6 \mu\text{H}/\text{m}$ and $C = 75.27 \text{ pF}/\text{m}$. In this specific scheme, the length of the symmetric transmission lines is set to $500 \mu\text{m}$. Note that $L1$, $C1$, $L2$, and $C2$ constitute bias-tee elements. Their values are selected arbitrarily.

detection at the center of the meander (the two nanowire transmission lines are symmetric).

APPENDIX C: NANOFABRICATION

We fabricate our differential SNSPDs on 100-mm silicon wafers, using a Canon EX3 DUV stepper [35] to fabricate about 200 SNSPDs per wafer. We begin by lifting off a patterned Ti/Au/Ti mirror, with 80-nm-thick Au. The Ti layers increase adhesion between the metals and dielectrics but are kept thin (approximately 1–2 nm) due to the better performance of Au as a mirror at around 1550 nm. A spacer layer of SiO₂ is then blanket rf bias sputtered on top of the mirrors while the substrate holder is biased at 375 kHz to produce a smoother SiO₂ film. The JPL NbN superconducting layer is subsequently deposited by reactive-sputtering a Nb sputtering target in a N₂–Ar gas mixture, while applying a rf bias to the substrate to reduce the grain size in the films following Ref. [56]. The dc power applied to the Nb target is 340 W, and the rf bias is 6–7 W. The films are deposited over a fixed time of 13 s, which gives an approximately-7-nm-thick film based on ellipsometry of similar films on SiO₂-on-Si wafers. NbN films at MIT are made using the same setup as reported in Ref. [56]. The resulting film is approximately 7 nm thick, determined through measurements of the sheet resistance and comparison with similar films deposited on SiO₂/Si. We next fabricate Ti/Au/Ti bond pads, using ion milling before Ti/Au/Ti electron-beam evaporation in order to produce good contact with the NbN. We use electron-beam lithography to write the nanowires and tapers simultaneously. The wafer with JPL NbN uses negative-tone resist, while the MIT wafer uses positive-tone resist. The JPL NbN films are etched in a mixture of CCl₂F₂, CF₄, and O₂ in an inductively-coupled-plasma reactive-ion etcher, while the MIT films are etched with use of CF₄ plasma. A blanket film of approximately 100 nm of SiO₂ is deposited to protect the SNSPDs immediately after this etch and the removal of the electron-beam photoresist in solvent baths. We then expose a lift-off pattern in the stepper to define the remainder of the antireflection (AR) stack above the active area of the SNSPDs but away from the bond pads, to avoid wire bonding through thick dielectrics. The AR stacks on each of the three wafers are simulated by our using refractive-index data for each layer and are designed to maximize efficiency at 1550 nm. For two of the wafers, we fabricate a one-layer AR stack of SiO₂/TiO₂. For the third wafer considered here, we use a double-layer AR stack of SiO₂/TiO₂ to produce a narrower band at around 1550 nm. The one-layer AR stack is 271 nm/167 nm (SiO₂/TiO₂) for one wafer with the JPL NbN film. Meanwhile, a wafer with MIT NbN has a stack of 263 nm/184 nm. The thicknesses differ due to the difference in refractive indices between the JPL and MIT NbN films. The two-layer AR stack on the other wafer with JPL

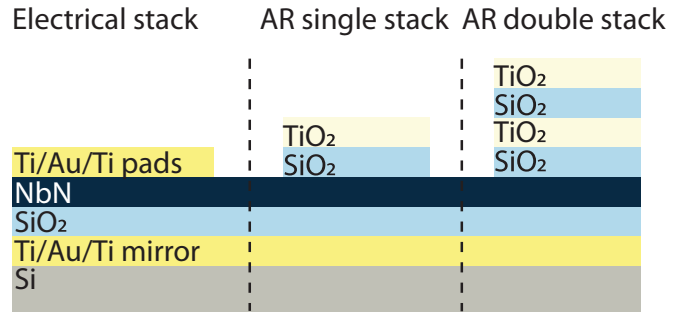


FIG. 12. The material stack.

NbN is approximately 150 nm/279 nm/157 nm/262 nm (SiO₂/TiO₂/SiO₂/TiO₂). Next, we write an etch-back pattern with the stepper and use the inductively-coupled-plasma reactive-ion etcher with CHF₃ and O₂ to etch through the blanket SiO₂ and spacer SiO₂. Finally, we expose an etch-back pattern and use deep reactive-ion etching to define the lollipop pattern that allows the detectors to be released from the wafer and inserted into zirconia sleeves for self-alignment to single-mode optical fibers [57]. We screen each detector at room temperature by probing the electrical resistance and measuring the reflection spectrum to determine the characteristics of the full optical cavity encompassing the mirror, spacer layer, NbN nanowires, and AR stack before testing. Figure 12 shows a sketch of the material stack.

APPENDIX D: MEASUREMENT SETUP AND CRYOGENIC READOUT

Figure 13 shows the experimental setups used for the characterization of our differential detectors. Table III provides an overview of the instrumentation [35]. In all the setups, the detectors are biased with a fully differential circuit. Moreover, for biasing as close as possible to the switching current and to avoid latching at high photon fluxes, we add cryogenic inductive shunts at both ports.

Figure 13(a) shows the experimental setup used for the characterization of the detector pulses, detector jitter t_{Σ} , differential time t_{Δ} histogram, and photon-number-resolution capabilities. Because of the impedance-matched design of the detectors, the signal amplitude is significantly increased, by as much as a factor of 3 compared with a regular SNSPD [26]. This results in a signal amplitude in the range of a few millivolts for both positive and negative pulses at the input of the first amplifier. To prevent saturation of the amplifier, a high-dynamic-range, single-stage cryogenic amplifier was developed by Cosmic Microwave Technology (CMTLF1s) [35]. The amplifier achieves a gain of 24 dB and a bandwidth of 2 GHz, while exhibiting a noise temperature of 4–7 K between 1 MHz and 2 GHz. The input power for 1-dB compression is –24 dBm. By using two of these amplifiers, one at each end of the

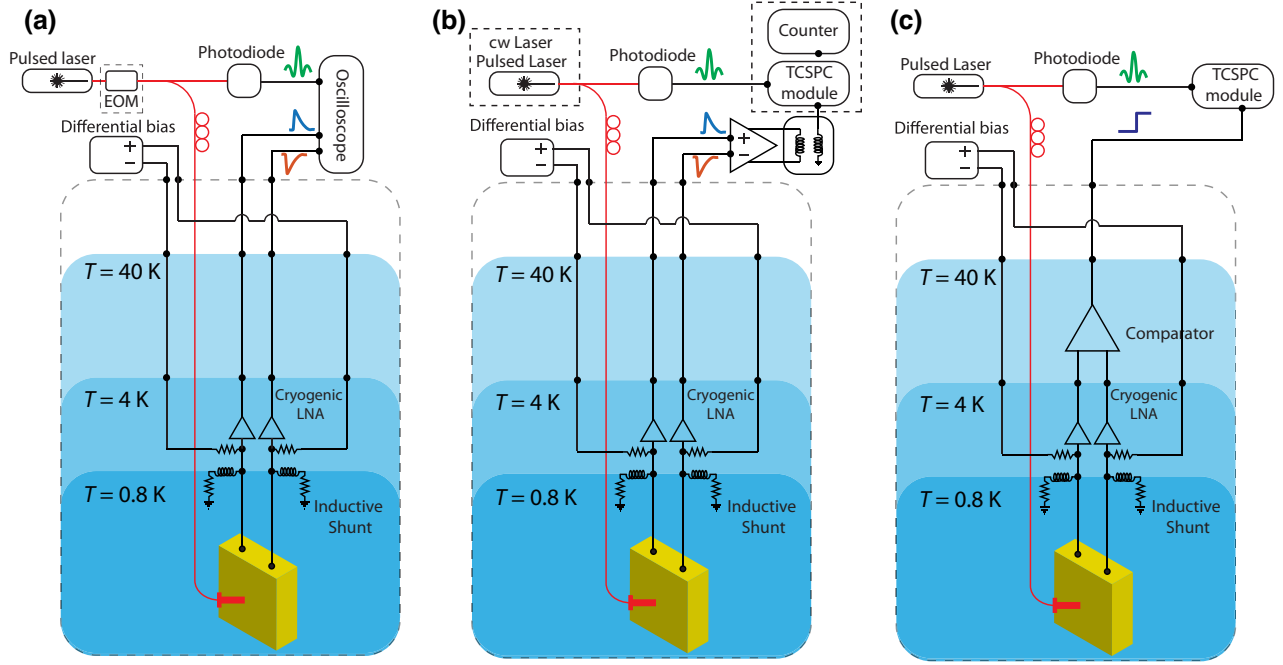


FIG. 13. Measurement setups. (a) Measurement setup for the characterization of the detector pulses, detector jitter t_{Σ} , differential time t_{Δ} histogram, and photon-number resolution. (b) Measurement setup for the characterization of the system detection efficiency and for the measurement of the system jitter j_{diff} using the balun in combination with the TCSPC module. (c) Measurement setup for the characterization of the system jitter j_{diff} using the cryogenic comparator in combination with the TCSPC module. LNA, low-noise amplifier.

differential detector, we verify that the dynamic range is sufficient to prevent saturation of the detector signal and that it maintains uniform gain for both positive and negative signals (see Fig. 4). After amplification, the detector outputs are directly interfaced with a real-time oscilloscope (Keysight DSOZ634A) [35], which we use to acquire the traces for postprocessing. To increase the SNR and reduce the impact of the electrical noise, the trigger is set on the steepest part of the pulse rising edge. The oscilloscope sampling rate is set to $80 \times 10^9\text{ s}^{-1}$ to minimize quantization error. The analog bandwidth was set to 6 GHz [5]. To measure the photon-number-resolution capabilities, the pulsed-laser repetition rate is reduced to 1 MHz with an intensity modulator.

The setup shown in Fig. 13(b) is used for the characterization of the system detection efficiency and for the measurement of the system jitter j_{diff} using the balun in combination with the TCSPC module. After amplification with the cryogenic low-noise amplifier, the detector outputs undergo a further stage of amplification through a low-noise differential amplifier (Analog Devices LTC6432-15) [35]. This is necessary to increase the signal level before the balun, which has a 6-dB insertion loss. From the differential amplifier, the outputs are connected to the balun board (Texas Instruments ADC-WB-BB) [35], which performs an operation equivalent to the difference of the complementary pulses. For the characterization of the

detection efficiency, the output of the balun is connected to a universal counter (Keysight 53220A) [35]. The detection efficiency is characterized after calibration of the optical-path losses. To measure the system jitter j_{diff} , the output of the balun is connected to the TCSPC module (Becker & Hickl SPC-150NXX) [35] together with a synchronization signal from the pulsed laser (Calmar Mendocino 1550 nm) [35] obtained with a fast photodiode.

The setup shown in Fig. 13(c) is used for the characterization of the system jitter j_{diff} using the cryogenic comparator in combination with the TCSPC module. After amplification with the cryogenic low-noise amplifiers, the detector outputs are fed to the differential comparator. The electronic circuit consists of a Si-Ge current-mode logic comparator thermalized at the 40-K stage of the cryostat. The offset of the input pulses is achieved with a pair of bias tees between the cryogenic amplifiers and the comparator. The output from the comparator is connected to the TCSPC module together with the synchronization signal.

APPENDIX E: ADDITIONAL DETAILS ON DIFFERENTIAL-DELAY-LINE IMAGING CAPABILITIES

Here we derive the first-order formula introduced in the main text to connect the characteristics of the t_{Δ}

TABLE III. Overview of the instruments.

Instrument	Model [35]
Cryogenic low-noise amplifier	Cosmic Microwave Technology CMTLF1s (1 MHz to 2 GHz)
Real-time oscilloscope	Keysight DSOZ634A (63 GHz)
Differential amplifier	Analog Devices LTC6432-15 (100 kHz to 1.4 GHz)
Balun board	Texas Instruments ADC-WB-BB/NOPB (4.5 MHz to 3 GHz)
Cryogenic comparator	Analog Devices HMC675LP3E
Inductive shunts	Custom: 1.1 μH + 50 Ω
Room-temperature amplifiers	Mini Circuits ZX60-P103LN+ (50 MHz to 3 GHz)
TCSPC module	Becker & Hickl SPC-150NXX
Photodiode	New Focus 1014 (45 GHz)
Pulsed laser	Calmar Mendocino 1550 nm, 10-MHz repetition rate
Universal counter	Keysight 53220A
Amplitude modulator	iXblue MXER-LN-20

histogram with effective mode misalignment on the meander ($\Delta x, \Delta y$). In Fig. 14(b) we analyze the condition in which the mode is vertically misaligned. In general,

$$\begin{aligned} t_{\Delta,1} &= \frac{L_m - 2x_p}{v_{\text{ph}}}, \\ t_{\Delta,2} &= \frac{L_m - 2(x_p + l(\Delta y))}{v_{\text{ph}}}, \end{aligned} \quad (\text{E1})$$

where $l(\Delta y) = W(w\Delta y)/F$ is the linearized length on the meander corresponding to Δy , as shown in Fig. 14(a). Here, w is the width of the nanowire, W the width of the meander, and F is the meander fill factor. The time-domain shift associated with $l(\Delta y)$ is

$$t_y = t_{\Delta,2} - t_{\Delta,1} = \frac{2l(\Delta y)}{v_{\text{ph}}} = \frac{2W}{v_{\text{ph}}} \frac{w\Delta y}{F}. \quad (\text{E2})$$

When $\Delta y = 0$, the peak of the envelope of the t_{Δ} histogram is at $t_{\Delta,1} = 0$. By rearranging Eq. (E2), we obtain a first-order formula to evaluate the vertical shift as a function of the peak of the envelope of the t_{Δ} distribution. Note that this derivation assumes $\Delta x = 0$, and it is therefore accurate within one meander pitch. In Fig. 14(c), we analyze the situation in which the mode is horizontally misaligned. In general,

$$\begin{aligned} t_{\Delta,0} &= \frac{L_m - 2x_p}{v_{\text{ph}}}, \\ t_{\Delta,-1} &= \frac{L_m - 2[x_p - (W - 2\Delta x)]}{v_{\text{ph}}}, \\ t_{\Delta,1} &= \frac{L_m - 2[x_p + (W + 2\Delta x)]}{v_{\text{ph}}}. \end{aligned} \quad (\text{E3})$$

The relative difference between adjacent histogram subpeaks is given by

$$\begin{aligned} t_x &= \Delta t_{\Delta,1,0} - \Delta t_{\Delta,0,-1} \\ &= (t_{\Delta,1} - t_{\Delta,0}) - (t_{\Delta,0} - t_{\Delta,-1}) \\ &= t_{\Delta,1} - 2t_{\Delta,0} + t_{\Delta,-1} \\ &= \frac{8\Delta x}{v_{\text{ph}}}. \end{aligned} \quad (\text{E4})$$

By rearranging Eq. (E4), we obtain a first-order formula to evaluate the horizontal shift as a function of the relative difference between adjacent histogram subpeaks.

APPENDIX F: ADDITIONAL DETAILS ON PHOTON-NUMBER RESOLUTION

We characterize the photon-number-resolution capabilities of our detector. We use the setup shown in Fig. 13(a). The repetition rate of our 1550-nm pulsed laser is 10 MHz. The reset time of our detector is approximately 160 ns.

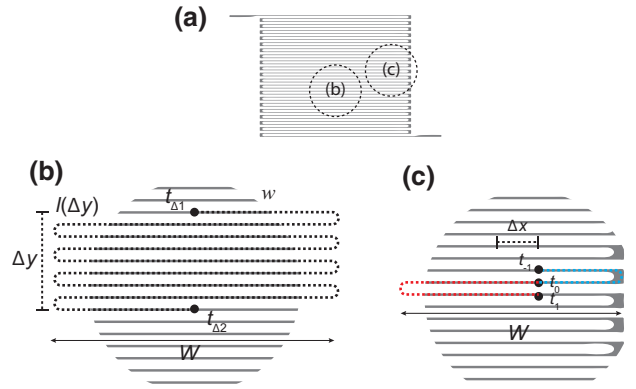


FIG. 14. Sketches for derivation of delay-line-imaging formulas. (a) Fiber spot misalignment reference on the meander for (b),(c). (b) The spot is vertically misaligned. (c) The spot is horizontally misaligned.

We use an intensity modulator to reduce the repetition rate of the laser to $f_{\text{rep}} = 1$ MHz to allow the detector to fully reset after a detection event. We estimate the effective photon number by measuring the output photon flux (Φ_q) and scaling it by the system detection efficiency (η_S) and the repetition rate:

$$\tilde{\mu} = \frac{\Phi_q}{f_{\text{rep}}} \eta_S. \quad (\text{F1})$$

Figure 15(a) shows the distribution of the peak of the difference of the complementary pulses for several effective photon numbers. Each distribution is fitted with up to four Gaussian functions. The counting statistics are reconstructed by integrating the areas under each Gaussian function. Notice that the fourth Gaussian function is introduced to fit the distribution for $\tilde{\mu} = 3.7$. We group the counting probability for $n \geq 3$ as these events are not well separated. For every effective mean photon number, the left shoulder is excluded from the fit. Note that for increasing photon number, the amplitude of the pulses increases.

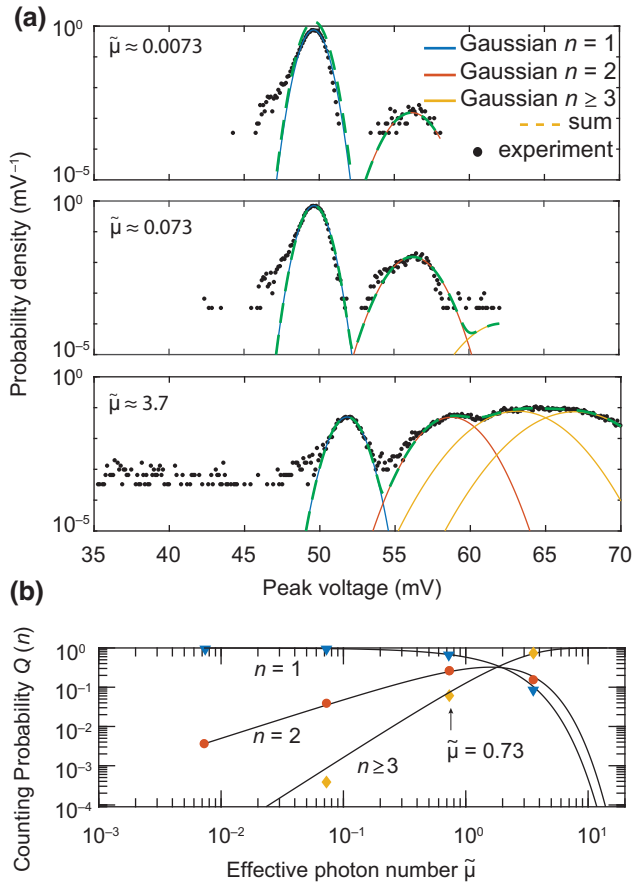


FIG. 15. Photon-number resolution. (a) Gaussian fitting of the pulse-amplitude histograms for several effective photon numbers. (b) Photon-counting statistics reconstructed from the pulse-height distributions under different illumination conditions.

In Fig. 15(b) we plot the counting probability $Q(n)$ (markers), extracted by our integrating the area under each Gaussian distribution, with the photon statistics of the coherent source $S(n) = e^{-\tilde{\mu}} \tilde{\mu}^n / n!$ (line). We group the probability for the events with $n \geq 3$, which are not clearly separated. In Fig. 15(b) we normalize the theoretical $S(n)$ by the probability of zero photons $S(n)/(1 - S(0))$, where $S(0) = e^{-\tilde{\mu}}$. Further details on the procedure are available in Ref. [6].

APPENDIX G: ESTIMATION OF UNCERTAINTIES

The uncertainties on the detector jitter j_Σ are estimated as the 95% confidence bound on the data. The uncertainties on the system jitter j_{diff} are mainly due to the resolution of the TCSPC module and are estimated as two time bins $\sigma_{\text{TCSPC}} = 0.4$ ps.

The system detection efficiency is estimated as follows:

$$\eta_S = \frac{C}{\Phi_q}. \quad (\text{G1})$$

where C is the count rate. We assume the uncertainty on the count rate to be negligible. The photon flux Φ_q is estimated as follows:

$$\Phi_q = \frac{P_0 A_1 A_2 A_3}{E_\lambda}, \quad (\text{G2})$$

where P_0 is the input optical power, measured with a calibrated power meter, A_1 , A_2 , and A_3 are the attenuation ratios of three optical attenuators used to attenuate the optical power, E_λ is the energy of the photon of wavelength λ . To measure the attenuation ratios A_1 , A_2 , and A_3 , the attenuators are connected in series and interfaced with the calibrated power meter through an optical switch. To measure the attenuation ratio, we set one of the attenuators to the desired value and the others to 0 dB. We measure the attenuated output power and we repeat the procedure for the other attenuators. A_1 , A_2 , and A_3 result from a relative measurement of the optical power using the same power meter. Therefore, to estimate the uncertainty on A_1 , A_2 , and A_3 , we consider only the relative uncertainty due to the nonlinearity $\sigma_{\text{NL}}(P)/P = 0.5\%$ on each measurement. The total uncertainty on the system detection efficiency is dominated by the power-meter uncertainty $\sigma(P)/P = 5\%$, and it is approximately $\sigma(\eta_S)/\eta_S = 5.2\%$.

- [1] D. V. Reddy, R. R. Nerem, S. W. Nam, R. P. Mirin, and V. B. Verma, Superconducting nanowire single-photon detectors with 98 system detection efficiency at 1550 nm, *Optica* **7**, 1649 (2020).
- [2] E. E. Wollman, V. B. Verma, A. D. Beyer, R. M. Briggs, B. Kozh, J. P. Allmaras, F. Marsili, A. E. Lita, R. Mirin, and

- S. Nam *et al.*, UV superconducting nanowire single-photon detectors with high efficiency, low noise, and 4 K operating temperature, *Opt. Express* **25**, 26792 (2017).
- [3] Y. Hochberg, I. Charaev, S. W. Nam, V. Verma, M. Colangelo, and K. K. Berggren, Detecting Sub-GeV Dark Matter with Superconducting Nanowires, *Phys. Rev. Lett.* **123**, 151802 (2019).
- [4] A. J. Kerman, D. Rosenberg, R. J. Molnar, and E. A. Dauler, Readout of superconducting nanowire single-photon detectors at high count rates, *J. Appl. Phys.* **113**, 144511 (2013).
- [5] B. Korzh *et al.*, Demonstration of sub-3 ps temporal resolution with a superconducting nanowire single-photon detector, *Nat. Photonics* **14**, 250 (2020).
- [6] D. Zhu, M. Colangelo, C. Chen, B. A. Korzh, F. N. Wong, M. D. Shaw, and K. K. Berggren, Resolving photon numbers using a superconducting nanowire with impedance-matching taper, *Nano Lett.* **20**, 3858 (2020).
- [7] R. H. Hadfield, Single-photon detectors for optical quantum information applications, *Nat. Photonics* **3**, 696 (2009).
- [8] A. Boaron *et al.*, Secure Quantum Key Distribution over 421 km of Optical Fiber, *Phys. Rev. Lett.* **121**, 190502 (2018).
- [9] H. Shibata, T. Honjo, and K. Shimizu, Quantum key distribution over a 72 dB channel loss using ultralow dark count superconducting single-photon detectors, *Opt. Lett.* **39**, 5078 (2014).
- [10] H. Takesue, S. W. Nam, Q. Zhang, R. H. Hadfield, T. Honjo, K. Tamaki, and Y. Yamamoto, Quantum key distribution over a 40-dB channel loss using superconducting single-photon detectors, *Nat. Photonics* **1**, 343 (2007).
- [11] F. Grünenfelder, A. Boaron, D. Rusca, A. Martin, and H. Zbinden, Performance and security of 5 GHz repetition rate polarization-based quantum key distribution, *Appl. Phys. Lett.* **117**, 144003 (2020).
- [12] R. Valivarthi, S. I. Davis, C. Peña, S. Xie, N. Lauk, L. Narváez, J. P. Allmaras, A. D. Beyer, Y. Gim, and M. Hussein *et al.*, Teleportation Systems toward a Quantum Internet, *PRX Quantum* **1**, 020317 (2020).
- [13] J. C. Chapman, T. M. Graham, C. K. Zeitler, H. J. Bernstein, and P. G. Kwiat, Time-Bin and Polarization Superdense Teleportation for Space Applications, *Phys. Rev. Appl.* **14**, 14044 (2020).
- [14] F. Samara, N. Maring, A. Martin, A. S. Raja, T. J. Kippenberg, H. Zbinden, and R. Thew, Entanglement swapping between independent and asynchronous integrated photon-pair sources, *Quantum Sci. Technol.* **6**, 045024 (2021).
- [15] F. Kaneda and P. G. Kwiat, High-efficiency single-photon generation via large-scale active time multiplexing, *Sci. Adv.* **5**, eaaw8586 (2019).
- [16] A. McCarthy, N. J. Krichel, N. R. Gemmell, X. Ren, M. G. Tanner, S. N. Dorenbos, V. Zwiller, R. H. Hadfield, and G. S. Buller, Kilometer-range, high resolution depth imaging via 1560 nm wavelength single-photon detection, *Opt. Express* **21**, 8904 (2013).
- [17] X. Wang, A. E. Dane, K. K. Berggren, M. D. Shaw, S. Mookherjea, B. A. Korzh, P. O. Weigel, D. J. Némchick, B. J. Drouin, W. Becker, Q. Y. Zhao, D. Zhu, and M. Colangelo, Oscilloscopic capture of greater-than-100 GHz, ultra-low power optical waveforms enabled by integrated electrooptic devices, *J. Light. Technol.* **38**, 166 (2020).
- [18] W. Becker, *Advanced Time-Correlated Single Photon Counting Techniques* (Springer, Berlin, 2005), Vol. 81.
- [19] J. Sutin, B. Zimmerman, D. Tyulmankov, D. Tamborini, K. C. Wu, J. Selb, A. Gulinatti, I. Rech, A. Tosi, D. A. Boas, and M. A. Franceschini, Time-domain diffuse correlation spectroscopy, *Optica* **3**, 1006 (2016).
- [20] M. Shaw, F. Marsili, A. Beyer, R. Briggs, J. Allmaras, and W. H. Farr, in *Free-Space Laser Communication and Atmospheric Propagation XXIX*, Vol. 10096, edited by H. Hemmati and D. M. Boroson, International Society for Optics and Photonics (SPIE, Bellingham, WA, 2017), p. 18.
- [21] Q. Y. Zhao, D. Zhu, N. Calandri, A. E. Dane, A. N. McCaughan, F. Bellei, H. Z. Wang, D. F. Santavicca, and K. K. Berggren, Single-photon imager based on a superconducting nanowire delay line, *Nat. Photonics* **11**, 247 (2017).
- [22] N. Calandri, Q. Y. Zhao, D. Zhu, A. Dane, and K. K. Berggren, Superconducting nanowire detector jitter limited by detector geometry, *Appl. Phys. Lett.* **109**, 152601 (2016).
- [23] I. Esmail Zadeh *et al.*, Efficient single-photon detection with 7.7 ps time resolution for photon-correlation measurements, *ACS Photonics* **7**, 1780 (2020).
- [24] V. Shcheslavskiy, P. Morozov, A. Divochiy, Y. Vakhtomin, K. Smirnov, and W. Becker, Ultrafast time measurements by time-correlated single photon counting coupled with superconducting single photon detector, *Rev. Sci. Instrum.* **87**, 53117 (2016).
- [25] By “single-pixel SNSPD,” we refer to nanowire detectors with active areas larger than $10 \times 10 \mu\text{m}^2$ (enough to contain the mode of a telecom fiber), and embedded in optical stacks tuned to maximize the system detection efficiency.
- [26] D. Zhu, M. Colangelo, B. A. Korzh, Q. Y. Zhao, S. Frasca, A. E. Dane, A. E. Velasco, A. D. Beyer, J. P. Allmaras, E. Ramirez, W. J. Strickland, D. F. Santavicca, M. D. Shaw, and K. K. Berggren, Superconducting nanowire single-photon detector with integrated impedance-matching taper, *Appl. Phys. Lett.* **114**, 042601 (2019).
- [27] A. J. Miller, A. E. Lita, B. Calkins, I. Vayshenker, S. M. Gruber, and S. W. Nam, Compact cryogenic self-aligning fiber-to-detector coupling with losses below one percent, *Opt. Express* **19**, 9102 (2011).
- [28] K. K. Berggren, Q. Y. Zhao, N. Abebe, M. Chen, P. Ravindran, A. McCaughan, and J. C. Bardin, A superconducting nanowire can be modeled by using SPICE, *Supercond. Sci. Technol.* **31**, 55010 (2018).
- [29] D. F. Santavicca, J. K. Adams, L. E. Grant, A. N. McCaughan, and K. K. Berggren, Microwave dynamics of high aspect ratio superconducting nanowires studied using self-resonance, *J. Appl. Phys.* **119**, 234302 (2016).
- [30] D. F. Santavicca, B. Noble, C. Kilgore, G. A. Wurtz, M. Colangelo, D. Zhu, and K. K. Berggren, Jitter characterization of a dual-readout SNSPD, *IEEE Trans. Appl. Supercond.* **29**, 1 (2019).
- [31] C. E. Marvinney, B. E. Lerner, A. A. Poretzky, A. J. Miller, and B. J. Lawrie, Waveform analysis of a large-area superconducting nanowire single photon detector, *Supercond. Sci. Technol.* **34**, 035020 (2021).

- [32] D. Zhu, Q. Y. Zhao, H. Choi, T. J. Lu, A. E. Dane, D. Englund, and K. K. Berggren, A scalable multi-photon coincidence detector based on superconducting nanowires, *Nat. Nanotechnol.* **13**, 596 (2018).
- [33] J. P. Allmaras, A. G. Kozorezov, B. A. Korzh, K. K. Berggren, and M. D. Shaw, Intrinsic Timing Jitter and Latency in Superconducting Nanowire Single-Photon Detectors, *Phys. Rev. Appl.* **11**, 34062 (2019).
- [34] S. Frasca, B. Korzh, M. Colangelo, D. Zhu, A. E. Lita, J. P. Allmaras, E. E. Wollman, V. B. Verma, A. E. Dane, E. Ramirez, A. D. Beyer, S. W. Nam, A. G. Kozorezov, M. D. Shaw, and K. K. Berggren, Determining the depairing current in superconducting nanowire single-photon detectors, *Phys. Rev. B* **100**, 054520 (2019).
- [35] Certain commercial equipment, instruments, or materials are identified in this paper to facilitate understanding. Such identification does not imply recommendation or endorsement by the National Institute of Standards and Technology, nor does it imply that the materials or equipment that are identified are necessarily the best available for the purpose.
- [36] E. Amri, G. Boso, B. Korzh, and H. Zbinden, Temporal jitter in free-running InGaAs/InP single-photon avalanche detectors, *Opt. Lett.* **41**, 5728 (2016).
- [37] M. J. Hsu, H. Finkelstein, and S. C. Esener, A CMOS STI-bound single-photon avalanche diode with 27-ps timing resolution and a reduced diffusion tail, *IEEE Electron Device Lett.* **30**, 641 (2009).
- [38] M. Sanzaro, P. Gattari, F. Villa, A. Tosi, G. Croce, and F. Zappa, Single-photon avalanche diodes in a 0.16 μm BCD technology with sharp timing response and red-enhanced sensitivity, *IEEE J. Sel. Top. Quantum Electron.* **24**, 1 (2018).
- [39] C. Bruschini, H. Homulle, I. M. Antolovic, S. Burri, and E. Charbon, Single-photon avalanche diode imagers in biophotonics: Review and outlook, *Light: Sci. Appl.* **8**, 87 (2019).
- [40] P. Ravindran, R. Cheng, H. Tang, and J. C. Bardin, Active quenching of superconducting nanowire single photon detectors, *Opt. Express* **28**, 4099 (2020).
- [41] A. N. McCaughan and K. K. Berggren, A superconducting-nanowire three-terminal electrothermal device, *Nano Lett.* **14**, 5748 (2014).
- [42] A. N. McCaughan, N. S. Abebe, Q.-Y. Zhao, and K. K. Berggren, Using geometry to sense current, *Nano Lett.* **16**, 7626 (2016).
- [43] M. Colangelo, D. Zhu, D. F. Santavicca, B. A. Butters, J. C. Bienfang, and K. K. Berggren, Compact and Tunable Forward Coupler Based on High-Impedance Superconducting Nanowires, *Phys. Rev. Appl.* **15**, 024064 (2021).
- [44] A. Wagner, L. Ranzani, G. Ribeill, and T. Ohki, Demonstration of a superconducting nanowire microwave switch, *Appl. Phys. Lett.* **115**, 172602 (2019).
- [45] S. Bartolucci, P. M. Birchall, M. Gimeno-Segovia, E. Johnston, K. Kieling, M. Pant, T. Rudolph, J. Smith, C. Sparrow, and M. D. Vidrighin, Creation of entangled photonic states using linear optics, arXiv preprint [arXiv:2106.13825](https://arxiv.org/abs/2106.13825) (2021).
- [46] M. Cattaneo, M. G. Paris, and S. Olivares, Hybrid quantum key distribution using coherent states and photon-number-resolving detectors, *Phys. Rev. A* **98**, 012333 (2018).
- [47] Y.-G. Shan, G.-J. Fan-Yuan, S. Wang, W. Chen, D.-Y. He, Z.-Q. Yin, G.-C. Guo, and Z.-F. Han, Characterizing photon-number distribution of pulsed sources using non-photon-number-resolving detectors for quantum key distribution, *Phys. Rev. A* **104**, 032406 (2021).
- [48] J. L. O'Brien, Optical quantum computing, *Science* **318**, 1567 (2007).
- [49] E. Knill, R. Laflamme, and G. J. Milburn, A scheme for efficient quantum computation with linear optics, *Nature* **409**, 46 (2001).
- [50] P. Kok, W. J. Munro, K. Nemoto, T. C. Ralph, J. P. Dowling, and G. J. Milburn, Linear optical quantum computing with photonic qubits, *Rev. Mod. Phys.* **79**, 135 (2007).
- [51] G. G. Taylor, A. McCarthy, B. Korzh, A. D. Beyer, D. Morozov, R. M. Briggs, J. P. Allmaras, B. Bumble, M. D. Shaw, R. H. Hadfield, and G. S. Buller, in *Conference on Lasers and Electro-Optics, OSA Technical Digest* (Optica Publishing Group, San Jose (CA), 2020), p. SM2M-6. https://opg.optica.org/abstract.cfm?uri=CLEO_SI-2020-SM2M.6.
- [52] S. I. Davis, A. Mueller, R. Valivarthi, N. Lauk, L. Narvaez, B. Korzh, A. D. Beyer, O. Cerri, M. Colangelo, and K. K. Berggren *et al.*, Improved Heralded Single-Photon Source with a Photon-Number-Resolving Superconducting Nanowire Detector, *Phys. Rev. Appl.* **18**, 064007 (2022).
- [53] J. Glasby, F. Faramarzi, S. Sytkens, P. Day, K. Berggren, and P. Mausekopf, Probing kinetic inductance pulses below the hotspot activation threshold of a superconducting nanowire, *IEEE Trans. Appl. Supercond.* **31**, 1 (2021).
- [54] A. N. McCaughan, A. N. Tait, S. M. Buckley, D. M. Oh, J. T. Chiles, J. M. Shainline, and S. W. Nam, PHIDL: Python-based layout and geometry creation for nanolithography, *J. Vac. Sci. Technol. B, Nanotechnol. Microelectron.: Mater. Process., Meas., Phenom.* **39**, 062601 (2021).
- [55] A. J. Kerman, J. K. Yang, R. J. Molnar, E. A. Dauler, and K. K. Berggren, Electrothermal feedback in superconducting nanowire single-photon detectors, *Phys. Rev. B - Condens. Matter Mater. Phys.* **79**, 100509(R) (2009).
- [56] A. E. Dane, A. N. McCaughan, D. Zhu, Q. Zhao, C. S. Kim, N. Calandri, A. Agarwal, F. Bellei, and K. K. Berggren, Bias sputtered NbN and superconducting nanowire devices, *Appl. Phys. Lett.* **111**, 122601 (2017).
- [57] V. B. Verma, F. Marsili, B. Baek, A. E. Lita, T. Gerrits, J. A. Stern, R. P. Mirin, and S. W. Nam, 55 system detection efficiency with self-aligned WSi superconducting nanowire single-photon detectors, *Opt. InfoBase Conf. Pap.*, 1 (2012).